Nuclear Engineering and Technology 55 (2023) 493–505

Contents lists available at ScienceDirect

Nuclear Engineering and Technology

journal homepage: www.elsevier.com/locate/net

Original Article

Deep-learning-based system-scale diagnosis of a nuclear power plant with multiple infrared cameras

Ik Jae Jin, Do Yeong Lim, In Cheol Bang*

Department of Nuclear Engineering Ulsan National Institute of Science and Technology (UNIST), 50 UNIST-gil, Ulju-gun, Ulsan, 44919, Republic of Korea

ARTICLE INFO

Article history:
Received 26 April 2022
Received in revised form
6 October 2022
Accepted 12 October 2022
Available online 15 October 2022

Keywords:
System scale diagnosis
Nuclear power plant
Infrared sensor
Deep learning
Convolutional neural network
Fault detection

ABSTRACT

Comprehensive condition monitoring of large industry systems such as nuclear power plants (NPPs) is essential for safety and maintenance. In this study, we developed novel system-scale diagnostic technology based on deep-learning and IR thermography that can efficiently and cost-effectively classify system conditions using compact Raspberry Pi and IR sensors. This diagnostic technology can identify the presence of an abnormality or accident in whole system, and when an accident occurs, the type of accident and the location of the abnormality can be identified in real-time. For technology development, the experiment for the thermal image measurement and performance validation of major components at each accident condition of NPPs was conducted using a thermal-hydraulic integral effect test facility with compact infrared sensor modules. These thermal images were used for training of deep-learning model, convolutional neural networks (CNN), which is effective for image processing. As a result, a proposed novel diagnostic was developed that can perform diagnosis of components, whole system and accident classification using thermal images. The optimal model was derived based on the modern CNN model and performed prompt and accurate condition monitoring of component and whole system diagnosis, and accident classification. This diagnostic technology is expected to be applied to comprehensive condition monitoring of nuclear power plants for safety.

1. Introduction

A nuclear power plants (NPPs) consist of several components for safety, which are monitored by the operator. Because NPP has so many important variables which change minutely or rapidly, monitoring the condition of NPP in a transient state by an operator sometimes leads to mistakes [1]. For example, in the Three Mile Island (TMI-2) unit 2 accident in 1979, a severe accident and core damage occurred by the operator's wrong decisions with equipment failures because the state of NPP could not be fully understood due to insufficient state information. The lesson of this case is that having a measurement method with additional, different mechanisms can help reduce human error by providing the information in different point of view. Accurate diagnosis of the condition of NPPs and identification of the cause and location of the accident can increase the probability of preventing damage to the core by making it easier for operators to recognize and address the problem. Therefore, along with the system diagnosis method of the existing nuclear power plant, the method of assisting the operator in monitoring the system in the transient state is essential to increase the safety of the nuclear power plant. In this regard, this study proposes a novel system monitoring technology that combines thermal image measurement using small-scale and broad-view infrared (IR) technology and a deep learning-based condition classification model. In this technology, each major component is visualized in real time with an IR camera, and the deep learning model determines whether each component and the entire system is abnormal by using the measured infrared thermal image, if an accident occurs, it determines the type and main location of the accident.

Deep learning technology is a method of machine learning that gradually learns meaningful features in successive deep neuron layers, and has strength in image data processing in particular. This has greatly advanced in the direction of faster and more accurate classification of data that is difficult or ambiguous for humans [2]. In the field of nuclear, studies using deep learning have been recently conducted in a variety of ways, and in particular, many studies have been conducted to diagnose the transient state of NPPs. For example, the prediction of critical heat flux by an artificial

---

* Corresponding author.
E-mail address: icbang@unist.ac.kr (I.C. Bang).

https://doi.org/10.1016/j.net.2022.10.012

neural network (ANN) was found to be faster than the prediction of system code using correlation [3], and ANN was used to diagnose NPP transients based on initial conditions of transients [4]. To validate the possibility of diagnosing and classifying transient conditions with deep learning, the state of an NPP was classified using a convolutional neural network (CNN), which was trained and evaluated using the reshaped results of the RELAP [5] calculation. In addition, deep learning technology has also been applied to real-time diagnostic studies that require fast computation, which it has proven its ability to reduce operator intervention. Lee et al. demonstrated the feasibility of real-time diagnosis of an NPP to classify the operating condition using the safety analysis code calculation results, which were utilized to train and test a two-channel CNN [6]. This can prevent operator-induced accidents and enable accident classification with a short response time. However, although several studies have attempted to incorporate deep learning into the safety of NPPs, most of studies have been based on results calculated using the safety analysis code. Studies that trained and evaluated the classification model using results of the system analysis code is meaningful in that it suggests a new possibility, but it is difficult to evaluate its practical applicability. Therefore, in order to evaluate the practical performance of deep learning technology, training using experimental data and applying it to an experimental facility is essential to evaluate its applicability.

In addition, because numerous measured values obtained by data-driven monitoring can cause confusion of the operators and result in difficulty locating faults or failures, intuitive non-contact IR thermography condition monitoring is widely accepted for the detection of malfunctions in machines or components [7]. Among deep learning techniques, CNNs have shown outstanding performance for processing images. The significant benefit of CNNs is that they require fewer parameters than an ANN, making it possible to classify more complex data accurately with a short response time [8]. The performance improvement of CNNs has allowed component-scale fault detection studies. For example, an application for fault detection of a rotating component using IR thermal technology and the CNN was proposed by demonstrating the feasibility of component diagnosis with a thermal image combined with deep learning [9]. A study was conducted to classify the state of a wiring device using an IR camera with the object detection method, which is a type of CNN, because diagnosis based on vibration requires direct contact with the device [10]. A health monitoring method for a radiator, which is a type of heat exchanger, was employed to classify the status of the radiator using an IR camera and visual geometry group (VGG) net, which is a CNN classification model [11]. In addition, owing to the limitation of crack detection by conventional cameras, crack detection was carried out using an IR camera and a deep learning object detection method [12].

Fault detection using IR cameras has been proposed in many industrial fields, and prompt and accurate component-scale classification was possible with the use of deep learning. Visual inspection of a component using an IR thermal camera with deep learning can be performed even when no measuring instrument is installed. However, because the deep-learning-based IR diagnostic technology uses a high-performance/high-resolution IR camera, it is not easy to install, difficult to transmit data, and need to a lot of budgets. In the case of deep learning-based IR diagnostic study for a single component, a commercial IR camera was used, and the price of one IR thermal camera used in the literatures was close to $10,000. Despite the high price, data transmission is not easy and requires a high-performance computing system. As a result, there was a disadvantage in that an additional cost was generated for data acquisition. Therefore, IR diagnostic technologies cannot be extended from component-scale diagnosis to system-scale diagnosis and have been used only for single-component subclassification. Nevertheless, using a single component is uncommon in many industries that use components. In order to overcome the difficulties of the above IR technology studies, this study utilized Raspberry Pi, a low-cost computing system, and a small IR sensor costing about $80 each, demonstrating similar diagnostic results compared to conventional analysis methods, and classifying accidents by enabling multi-component diagnosis at a low cost. If deep-learning-based IR technology could diagnose multiple components, improved safety could be realized by an intuitive diagnostic method not only for nuclear power plants but also for many industrial fields.

This study utilizes small IR thermal cameras and a Raspberry Pi, which can facilitate installation, data transmission, and cost-effectiveness to overcome the limitations of expanding to the system scale. Therefore, a deep-learning-based system-scale diagnosis method using IR thermal cameras is proposed for component diagnosis and accident classification. The data for system-scale diagnosis were generated using IR thermal cameras based on the experimental data of the UNIST reactor innovative loop (URI-LO) which is a scaled-down thermal-hydraulic experimental NPP facility [13]. The CNN deep learning classification model was trained using thermal images of major URI-LO components for accurate component diagnosis and accident classification in quasi-real-time.

2. Modeling and methodology

In contrast to previous studies that used safety analysis codes with AI for the diagnosis of NPPs, this study trained and tested the deep learning model using data obtained from the integral test facility, URI-LO, which scales down APR 1400 (1/8 height, 1/12 diameter), to ensure the reliability of the deep learning model. URI-LO is shown in Fig. 1. The steady-state operation condition was designed using the three-level scaling method proposed by Ishii and Kataoka [14]. The design operating conditions are listed in Table 1.

The transient data for the deep learning model were obtained through experiments based on the design operating conditions of URI-LO. Considering the application of the proposed IR technology to various industries, this study was carried out by combining a Raspberry Pi and compact IR thermal cameras, which are convenient to install, transmit data, and are cost-effective. After the state of the main component was diagnosed, early-stage accident classification based on diagnosed component data was developed through deep learning using small IR cameras. The reactor coolant pump (RCP) and secondary side of the steam generator, which change significantly at the early stage of transient conditions, were considered for system-scale diagnosis. The classified accidents include both design-basis accidents (DBAs) and beyond-design-basis accidents (BDBAs). A DBA is a postulated accident that a nuclear facility must be designed and built to withstand without loss to the systems, structures, and components necessary to ensure public health and safety. BDBA is used as a technical means to discuss accident sequences that are possible but have not been fully considered in the design process.

2.1. Validation of the experiment based on the thermal-hydraulic analysis code

The thermal-hydraulic analysis code is frequently utilized to analyze transient conditions of NPPs or facilities. The calculation results of the multi-dimensional analysis of reactor safety (MARS) thermal analysis code have shown similar behavior to the experimental transient conditions [16–18]. The accidents to be classified using the deep learning model were analyzed with the MARS code

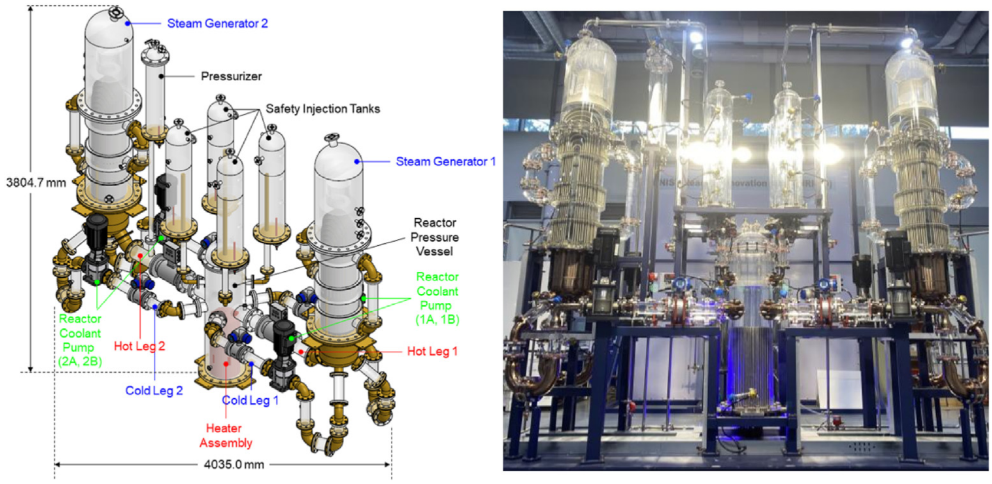

Fig. 1. Schematics of URI-LO

Table 1
Designed normal operation conditions for URI-LO [15].

Design parameters	APR-1400	Scaling ratios (P/M)	URI-LO (Water)
RCS pressure [bar]	155.13	155.13	1.0
Core inlet temperature [^{o}C]	290.6	–	74.0
Core outlet temperature [^{o}C]	325.0	–	91.2
Temperature difference [^{o}C]	34.4	0.5	17.2
Core flow rate [kg/s]	550.6	203.9 $^{(C}p,oR^{l}oR^{1/2d}oR^{2)}$	2.7
Core power [MW]	79.66	$^{407.3\ (l}oR^{1/2d}oR^{2)}$	0.196
SG pressure [bar]	70.0	291.65	0.24
SG steam temperature [^{o}C]	291.0	–	66.0
SG heat removal [MW]	39.92	$^{407.3\ (l}oR^{1/2d}oR^{2)}$	0.098

to validate the URI-LO experiment. Because the MARS analysis results for URI-LO, an integral effect test facility, show transient behavior similar to that of NPPs or other integral effect test facilities [13], the experimental URI-LO results and MARS calculation results were compared. Transient condition analysis was carried out focusing on the RCP and steam generator water level, which are the main components to be diagnosed.

2.1.1. Simulation of RCP rotor seizure accident

RCP rotor seizure is a type of loss of flow accident, which is classified as a DBA. The URI-LO experiment of an RCP rotor seizure accident was carried out for Loops 1 and 2. However, the experimental and MARS code calculation results were compared only for the RCP rotor seizure in Loop 1 because the RCP rotor seizure in Loop 2 exhibited similar behavior to that of Loop 1. Although the significant transition caused by the RCP rotor seizure accident is a flow rate change for all RCPs, the water level in the steam generator secondary side does not fall significantly. A comparison between the MARS calculation results and experimental results for the RCP rotor seizure accident in Loop 1 is shown in Fig. 2(a). The flow rates of all RCPs were changed by the RCP rotor seizure accident. The flow rates of the 2A and 2B RCPs increased and then decreased, while the flow rates at the 1A and 1B RCPs decreased. The behaviors of the URI-LO experiment and the MARS code calculation were similar for RCP rotor seizure.

2.1.2. Simulation of SBO accident

Since the Fukushima Daiichi nuclear disaster, SBO has been considered a crucial accident and has been considered in behavioral analyses [19,20]. The significant early stage changes in each component during an SBO accident include the turning off of all RCPs and a collapse of the water level in the steam generator compared to normal operating conditions. Comparisons of the MARS analysis results and experimental results are shown in Fig. 2(b) and (c) for the main components diagnosed using the IR thermal cameras for accident classification. Based on the MARS analysis and URI-LO SBO experiment results, when SBO occurs, because the system operating power is no longer supplied, all off the RCPs cease operation, and the steam generator water level collapses in all loops because feedwater is no longer injected into the steam generator. Although the result of the URI-LO SBO simulation showed almost the same behavior as that of the MARS calculation, the flow rate of the experiment fluctuated more than the MARS calculation results.

2.2. Configuration of the small IR cameras

Because high-resolution IR cameras are difficult to install, have difficulty transmitting thermal data, and are costly, the use of existing IR technology to realize diagnosis at the system scale is difficult despite the non-contact and intuitive monitoring method. Therefore, this study proposes a method utilizing Raspberry Pi with compact IR thermal cameras, which have simple installation, use multi-remote control, and are cost-effective. The Raspberry Pi enables measurement of the IR intensities acquired from the compact IR sensors. To measure the IR data, the module for the IR sensor or general-purpose input/output (GPIO) connection can be used. However, the connection of the IR camera to the Raspberry Pi through the module was more stable than the GPIO connection. Fig. 3 shows a schematic of a compact IR thermal camera connected to the Raspberry Pi using the module. FLIR Lepton 3.5 is used as the compact IR thermal sensor. The performance of the FLIR Lepton 3.5 is summarized in Table 2.

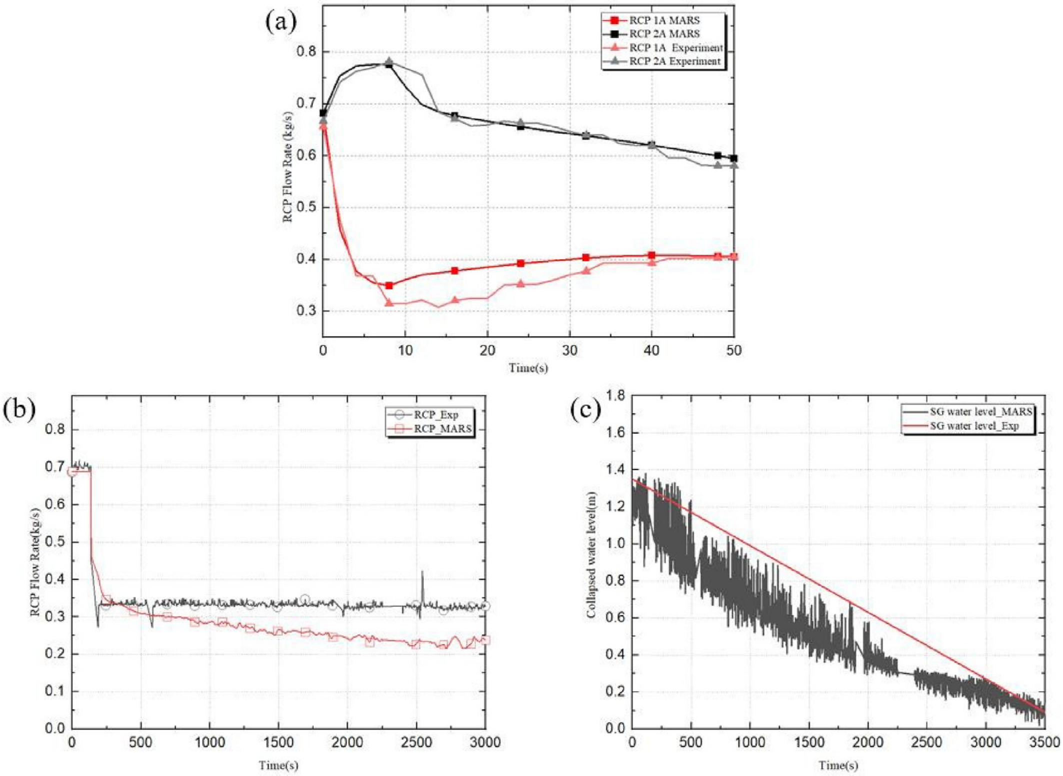

Fig. 2. Transient behavior in the MARS code calculation and URI-LO experiments: (a) RCP flow rate during an RCP rotor seizure accident, (b) RCP flow rate, and (c) collapsed water level of the steam generator secondary side during an SBO accident.

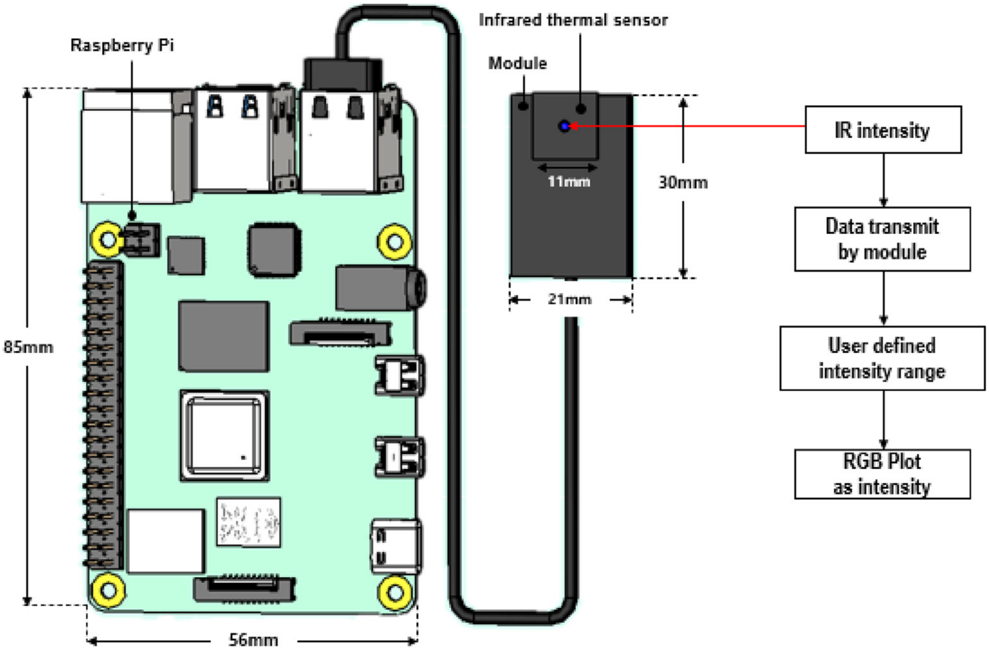

Fig. 3. Schematic of the IR thermal camera connected to the Raspberry Pi through the module.

The thermal image was created by measuring the intensity with a compact IR sensor using a Raspberry Pi. The IR intensity and range were adjusted to respond to even minute temperature changes. Fig. 4 shows a flowchart of the overall NPP component diagnosis and accident classification based on the IR cameras and deep learning. Each Raspberry Pi remotely controlled by the main control computer improved the controllability of the compact IR thermal cameras. The main components diagnosed using the IR thermal cameras with deep learning were the 1A, 1B, 2A, and 2B RCPs along with the water level of the steam generator in Loops 1 and 2. The

Table 2
Main features of the FLIR Lepton 3.5

FLIR Lepton 3.5	
Array format	*160 x 120, progressive scan*
Spectrum range	*Longwave infrared,* 8 µm *to* 14 µm
Pixel size	12 µm
Thermal sensitivity	< 50 mK *(0.050°C)*
Radiometric Accuracy	*+/- 5°C or 5%*
Scene dynamic range (High gain mode)	*- 10°C to + 140°C*
Scene dynamic range (Low gain mode)	*- 10°C to + 450°C*
Optimum operating temperature range	*−10°C to + 80°C*
Non-operating temperature range	*−40°C to + 80°C*

data were acquired with a Raspberry Pi from the IR thermal cameras, and major components were diagnosed using a model trained by deep learning on the Raspberry Pi. The thermal image diagnosed by deep learning was transmitted to the main control computer after post-processing. However, the component diagnosis time per thermal image by the trained model was 1.5144 s at the terminal of the Raspberry Pi. Therefore, component diagnosis by the Raspberry Pi terminal cannot realize real-time diagnosis owing to the long time required per component thermal image. For real-time diagnosis, this study employed the connection of the Raspberry Pi to a remote GPU server. The time required for diagnosis is reduced with connection to the remote GPU server. Remote GPU server allows users to log in to another computer, run commands on a remote system, and copy files to another system. When the Raspberry Pi was connected to the remote GPU server, the diagnosis time per thermal image decreased to 0.053348 s. The diagnosis time, which includes the pre-processing and post-processing times in the remote GPU server and Raspberry Pi terminal, is shown in Fig. 5. The connection could diagnose the main components with quasi-real-time performance, including the processing time.

2.3. Characteristics of the dataset

Although a large amount of steady-state data can be acquired conveniently during system operation, obtaining transient data from NPPs is difficult under artificial accidents. In addition, when a transient signal is generated, the reactor will be subject to a SCRAM because the reactor protection system (RPS) will be activated. Therefore, it is challenging to obtain data for transient situations. Hence, a deep learning model that is trained using a small amount of thermal image data should accurately classify the transient condition based on actual transient conditions. Owing to the automatic operation of the RPS, the thermal image data is composed of 2–3 s of each transient condition, which is diagnosed by the deep learning model. The experimental conditions verified in section 2.1 was repeated three times for each condition to database the thermal images of each component for deep learning application at failure condition. The amount of data for the state of each component is designated as 100 to verify the feasibility of high-performance system diagnosis by the deep learning model. The number of thermal images of each component and the number of accident data are given in Tables 3 and 4, respectively. The dataset was divided; 90% of the data was used as training and validation data, and 10% was used as test data. Of the 90%, 80% was used for training, and 20% was classified as validation data for the training process. In this study, considering the actual NPP situation, training was performed with a small amount of data. Therefore, data augmentation was carried out to prevent overfitting and improve the accuracy of the deep learning model.

2.4. Architecture of the CNN

Among deep learning architectures, CNNs exhibit effective image processing performance [8]. A CNN is trained by extracting patterns from images while processing the images. Therefore, a CNN was used to classify the thermal images for diagnosis of the NPP system. There are numerous types of CNNs, such as classification, object detection, and segmentation. A classification-type CNN architecture is used in this study because the deep learning model is intended to classify the data acquired by fixed IR cameras, and each thermal image contains one main component. The main components comprising the NPP should be diagnosed accurately and promptly to increase the safety of the NPP. Hence, a classification algorithm that has a short test time and high accuracy for thermal images is required for the system diagnosis. Classifying the type of accident for a large-scale system composed of numerous components by diagnosing only the components is challenging. Therefore, we propose an accident classification method using diagnosed thermal images with deep learning after the application of component diagnosis. A schematic of the CNN models is shown in Fig. 6.

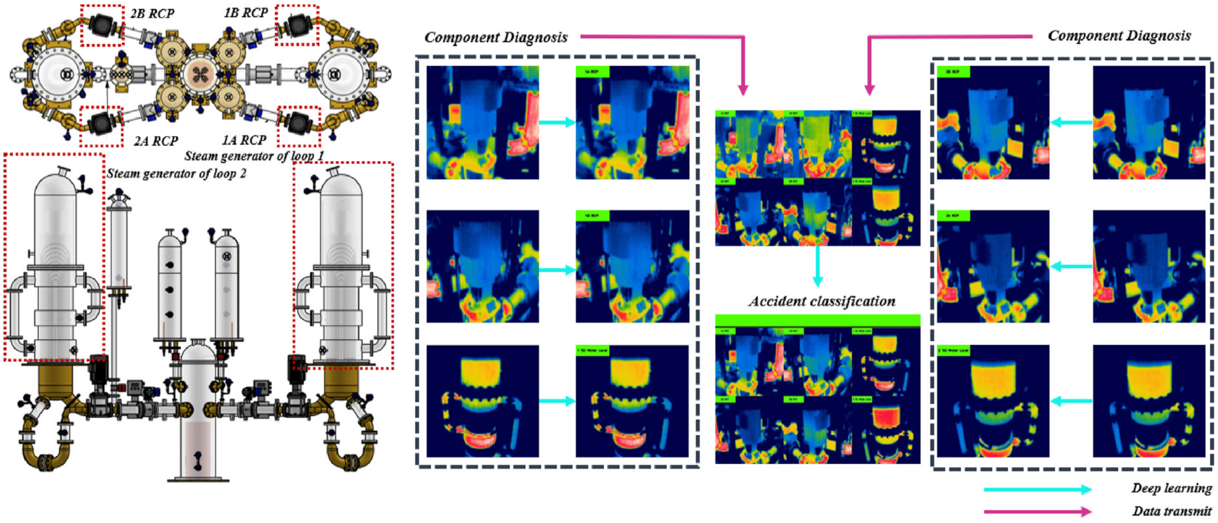

Fig. 4. Schematic of the system scale diagnosis by deep learning with IR thermal images.

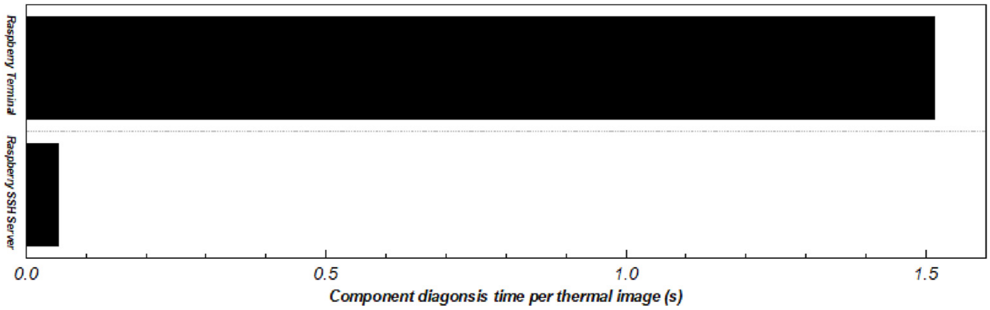

Fig. 5. Comparison of the diagnosis times per thermal image with the Raspberry Pi terminal and remote GPU server.

Table 3
Thermal image dataset for training of the component diagnosis model.

	Total Data	Training Data	Validation Data	Test data	Pixel size
1A RCP Normal	*100*	*72*	*18*	*10*	*224 × 224 × 3*
1A RCP Abnormal	*100*	*72*	*18*	*10*	*224 × 224 × 3*
1B RCP Normal	*100*	*72*	*18*	*10*	*224 × 224 × 3*
1B RCP Abnormal	*100*	*72*	*18*	*10*	*224 × 224 × 3*
Normal water level of steam generator 1	*100*	*72*	*18*	*10*	*224 × 224 × 3*
Collapsed water level of steam generator 1	*100*	*72*	*18*	*10*	*224 × 224 × 3*
2A RCP Normal	*100*	*72*	*18*	*10*	*224 × 224 × 3*
2A RCP Abnormal	*100*	*72*	*18*	*10*	*224 × 224 × 3*
2B RCP Normal	*100*	*72*	*18*	*10*	*224 × 224 × 3*
2B RCP Abnormal	*100*	*72*	*18*	*10*	*224 × 224 × 3*
Normal water level of steam generator 2	*100*	*72*	*18*	*10*	*224 × 224 × 3*
Collapsed water level of steam generator 2	*100*	*72*	*18*	*10*	*224 × 224 × 3*

Table 4
Thermal image dataset for training of the accident classification model.

	Total Data	Training Data	Validation Data	Test data	Pixel size
Normal operation	*100*	*72*	*18*	*10*	*672 × 448 × 3*
Loop 1 RCP rotor seizure	*100*	*72*	*18*	*10*	*672 × 448 × 3*
Loop 2 RCP rotor seizure	*100*	*72*	*18*	*10*	*672 × 448 × 3*
Station blackout	*100*	*72*	*18*	*10*	*672 × 448 × 3*

Various studies have been carried out and compared to develop better classification models [21]. Numerous classification architectures have been developed, such as AlexNet [22], GoogleNet [23], VGG net [24], ResNet [25], and DenseNet [26]. Selecting the optimal algorithm/structure for deep learning applications is important to prove the same performance when applied to other systems. In addition, the selection of the proper architecture is a significant effect on the application of the technique because it proves that the model could classify the state with high accuracy and optimal time for given data. Therefore, various architecture have been compared to implement an optimal classification model that enables prompt and accurate classification of thermal images. In addition, because the classification time depends on the architecture, in this study, ResNet, VGGNet, AlexNet, GoogleNet, DenseNet, and ANN were compared to select the optimal architecture for the thermal images. Table 5 represents the number of parameters and multiply and accumulate per sec (MACs) of the architecture for thermal imaging used in this study. MACs is related to classification time due to a unit used to confirm the performance of parameter computing. Because the performance of the deep learning model can change owing to the hyperparameters, the optimizer, learning rate, and batch size were adjusted to achieve the optimal hyperparameters for training, and the hyperparameters were applied to train the component diagnosis and accident classification CNN models. Adaptive momentum estimation (Adam) algorithm was used as the optimizer for this study [27]; learning rates of 0.001 were considered. Considering the amount of data, batch sizes of 4 was used. The training epoch was set to 100 to ensure high performance with little learning. The training conditions for the optimal architecture and hyperparameter selection are listed in Table 6. The training was carried out without pre-trained weight. The deep learning application was conducted based on the PyTorch, which is the deep learning framework on python. Because there is no possibility of classifying other components when using fixed IR cameras, each component in the normal and abnormal states is separately trained to prevent misdiagnosis as an incorrect component when the components are diagnosed using deep learning.

2.5. *Evaluation of the deep learning performance*

Based on a confusion matrix, model evaluation was performed for the thermal-image-based system-scale diagnosis. The classification performance of the test data was summarized by a confusion matrix. A confusion matrix is often used to evaluate classifiers that include two or more classes [28]. The confusion matrix is composed of positive and negative classes: true positive (TP), true negative (TN), false positive (FP), and false negative (FN). These parameters are defined as classifying a positive as a positive, classifying a negative as negative, classifying a negative as positive, and classifying a positive as negative, respectively. The performance of the

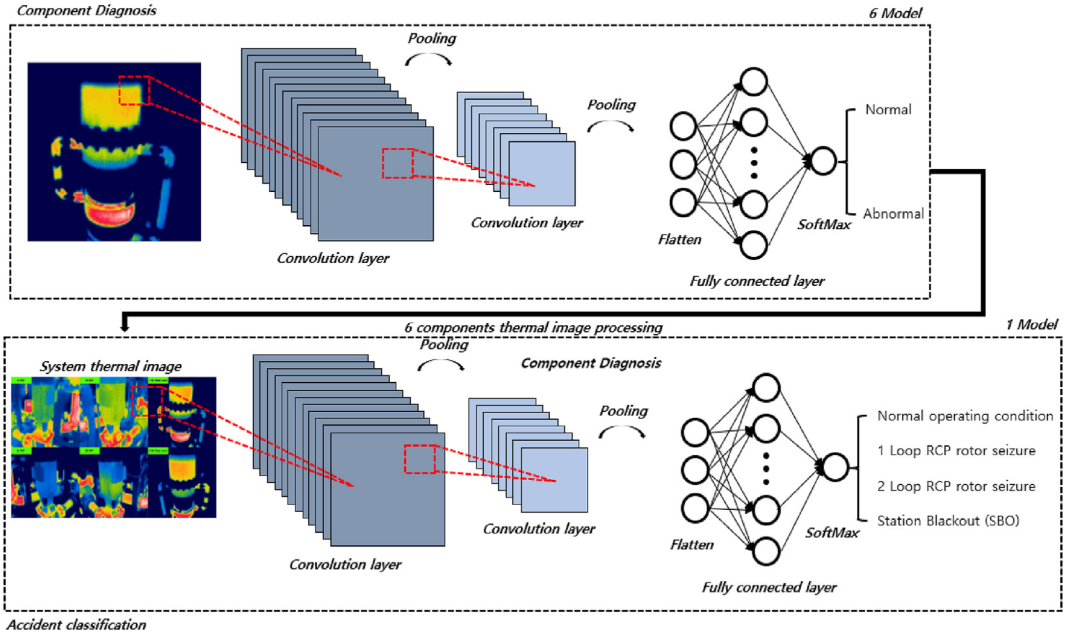

Fig. 6. Schematic of the total number of training models and training process for each model.

Table 5
The number of parameters and multiply and accumulate per sec of architectures for IR thermal images.

Architectures	Parameter	MACs
ANN (200, 200, 200)	60,373,204	30,186,000
ANN (300, 300, 300)	90,679,804	45,339,000
ANN (400, 400, 400)	121,066,404	60,532,000
ANN (500, 500, 500)	151,533,004	75,765,000
AlexNet	124,756,688	1,135,256,096
VGGNet-16	268,554,372	15,466,176,512
VGGNet-19	279,178,884	19,627,974,656
GoogLeNet	20,640,428	1,575,133,184
ResNet-18	22,355,076	1,813,562,368
ResNet-34	42,571,396	3,663,250,432
ResNet-50	47,024,260	4,087,140,352
ResNet-101	85,008,516	7,799,361,536
ResNet-152	116,295,812	11,511,582,720
DenseNet-101	1,580,564	416,052,624

CNN model was first evaluated based on the accuracy, recall, precision, and F1 score based on four factors. Accuracy represents the overall performance of the classifier. Recall represents the proportion of positive outcomes predicted by the model out of the actual positive outcomes. Precision represents the proportion of actual positive outcomes out of the outcomes classified as positive by the model. The F1 score represents the harmonic average, considering the precision and recall. These statistical parameters are described by Equations (1)–(4) [29].

$$Accuracy = \frac{TP + TN}{TP + TN + FP + FN} \tag{1}$$

$$Recall = \frac{TP}{TP + FN} \tag{2}$$

$$Precision = \frac{TP}{TP + FP} \tag{3}$$

$$F1\ score = 2* \frac{Precision*Recall}{Precision + Recall} \tag{4}$$

The trained models were compared in terms of the training loss, validation loss, and test loss to determine whether the models were over-fitted. If the validation loss and test loss did not converge, the model was considered over-fitted. If the model is over-fitted, it will

Table 6
Training conditions for selection of the optimal architecture and hyperparameter for component diagnosis and accident classification.

Architecture	Hidden layer	Optimizer	Learning rate	Loss function	Batch size	Epoch	Hardware
ANN	(200, 200, 200) (300, 300, 300) (400, 400, 400) (500, 500, 500)	Adam	0.001	Cross-entropy	4	100	GPU: Tesla-k80
AlexNet	AlexNet						
VGGNet	VGGNet-16 VGGNet-19						
GoogLeNet	GoogLeNet						
ResNet	ResNet-18 ResNet-34 ResNet-50 ResNet-101 ResNet-152						
DenseNet	DenseNet-101						

exhibit high accuracy for the training data. However, it will not be able to classify the new data. Hence, the model was evaluated at the lowest point of validation loss, considering the over-fitting of model. In addition, the occurrence of bias in the model can be evaluated by comparing the validation loss and test loss. In a biased model, even if either the validation loss or test loss is low, the other may be high. Therefore, convergence of the validation loss and test loss is considered to be important.

2.5.1. *k-fold cross validation*

Because the model in this study was trained and evaluated using a small amount of data, there was a possibility that the model may be biased even if the CNN model exhibited high performance. Therefore, k-fold cross-validation was performed on the model to verify the model performance. For k-fold cross-validation, the entire dataset is divided into k groups. Then, the model is trained using k-1 groups and evaluated using the remaining group. After k iterations of training and evaluation, the model performance is evaluated based on the confusion matrix. Here, k values of 2, 5, 8, and 10 were considered, and the evaluation was carried out for all k.

2.5.2. *Grad-CAM*

The method of creating visual explanations for the results of CNN-based models makes CNN-based models more transparent and explanatory. Gradient-weighted Class Activation Mapping (Grad-CAM) could be applied to most CNN architectures for the application of the method and does not require a separate architectural change or re-training [30]. Grad-CAM uses the gradient of the target concept flowing to the final convolutional layer to create a coarse localization map that emphasizes important parts of the image when predicting. Therefore, Grad-CAM facilitates knowing which part of the image the neural network looked at and made a judgment based on a specific label. CAM is a very useful tool to open the inside of CNN. In this study, an analysis of the pattern extracted through Grad-CAM was carried out with the trained model to perform a more in-depth study on the outcomes.

3. Results and discussion

3.1. *IR thermography*

Thermal images for the normal and abnormal states of the main components to be diagnosed for accident classification are shown in Fig. 7, which were acquired by compact IR cameras. The thermal images of the RCPs under normal operation are shown in Fig. 7(a), (c), (g), and (i). The thermal images of RCPs that are not operating owing to rotor seizure or power cut-off are shown in Fig. 7(b), (d), (h), and (j). Thermal images obtained when the water level of the steam generator is in the normal range with normal operation of the feedwater injection are shown in Fig. 7(e) and (k). Thermal images obtained when the water level of the steam generator has fallen outside the normal water level without feedwater injection are shown in Fig. 7(e) and (k). The heat generated by the pump operation was sufficiently reduced to allow normal operation of the pump to be distinguished as soon as the pump stopped working, regardless of any accidents. In classifying the water level of the steam generator through thermal images, the operator could not distinguish the difference between the normal water level and low water level when the feed water was not injected, despite the more intuitive monitoring method than conventional data-driven methods. Therefore, deep learning for component diagnosis was employed to distinguish differences that were difficult for humans to identify. The thermal images of components diagnosed by the deep learning model were post-processed, and all of the thermal images were then transmitted to the main control computer to enable monitoring of the entire system. The diagnosed components were displayed in green when operating normally and red when outside the normal range to assist the system operator. Fig. 8 shows the combined thermal images for system monitoring in the normal state and during an RCP rotor seizure accident of Loop 1, RCP rotor seizure accident of Loop 2, and SBO accident. The combined thermal images of components diagnosed by deep learning can allow the problem location to be identified more intuitively than with the existing methods. However, if intervention of the system operator becomes essential to classify the accident, the possibility of misclassification still remains. Moreover, if the number of components is increased, prompt accident classification becomes difficult at an early stage, and deep learning is utilized to classify the accident situation.

3.2. *Deep learning performance evaluation*

The CNN models for all pump diagnoses and accident classifications showed good performance, regardless of the CNN algorithm in most cases. To the extent to which human eyes could confirm, the CNN model was easily trained. In addition, in the case of the accident classification model, post-processing of the thermal images of the main components was performed to give the CNN model an advantage during training, resulting in high performance. However, there was a significant difference depending on the architecture utilized when training the steam generator water level diagnosis. Therefore, the optimal architecture for thermal images were determined using the steam generator water level diagnosis data.

3.2.1. *Architecture selection*

The CNN structure for the optimal model was implemented and trained under the same conditions, i.e., the same method of receiving data, data augmentation process, and hyperparameters. The batch size was set to 4, the optimizer was Adam, and the learning rate was set to 0.001. The accuracy of the validation and test data for all of the compared structures is shown in Fig. 9. Because not only accuracy but also the convergence of loss and prompt diagnosis were considered important for model performance, Table 7 summarizes the losses and diagnosis time per thermal image with post-processing for each structure. The performance of each architecture was summarized in Table 8. The diagnostic performance for most architectures was outstanding, which is considered due to the property of the dataset used for this study. In this study, the IR sensors were fixed to diagnose each component. Due to the stationary, component size, angle, etc. in the thermal image did not change, which improved the diagnostic performance. Therefore, it is considered that the diagnosis using the fixed thermal image could contribute to the performance enhancement for component diagnosis.

ANN_200, ANN_300, ANN_400, and ANN_500 indicate hidden layers of (200, 200, 200), (300, 300, 300), (400, 400, 400), and (500, 500, 500), respectively. All of the ANNs and AlexNet had the fastest diagnosis times, but the accuracy of the validation and test data was low, and training did not proceed without the convergence of all types of losses. Although VGG Net 16 had high accuracy for the validation data with a prompt diagnosis distinct from VGG Net 19, it had poor diagnostic performance for the test data. Among the ResNet architectures, the performance of ResNet 34 was more suitable for the diagnosis or classification of thermal images than the other ResNet types. GoogLeNet demonstrated good performance for all of the thermal imaging diagnoses with prompt classification. DenseNet also showed good performance for thermal images, but its performance was lower than those of GoogLeNet and ResNet 34. Both GoogLeNet and ResNet 34 showed good

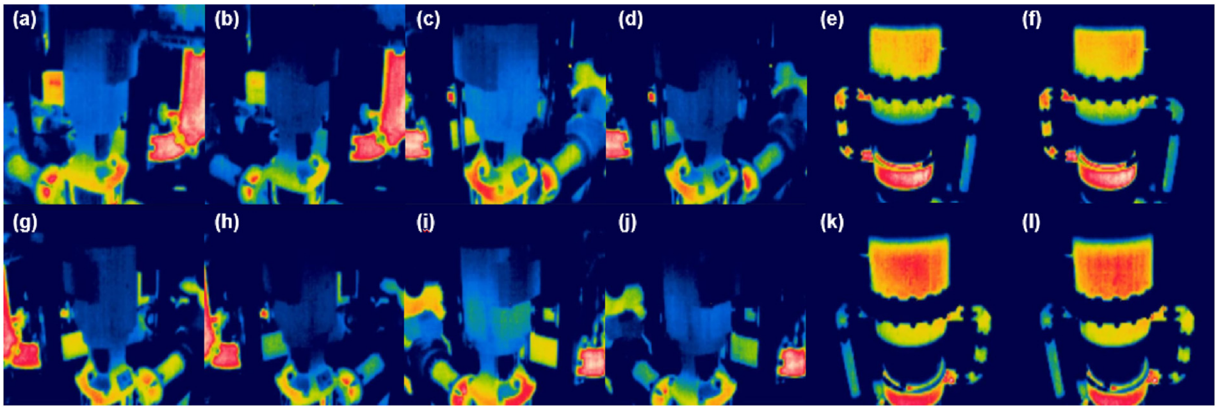

Fig. 7. Thermal images acquired by compact IR cameras: (a) 1A coolant pump [normal], (b) 1A coolant pump [failed], (c) 1B coolant pump [normal], (d) 1B coolant pump [failed], (e) Loop 1 steam generator [normal water level], (f) Loop 1 steam generator [collapsed water level], (g) 2A coolant pump [normal], (h) 2A coolant pump [failed], (i) 2B coolant pump [normal], (j) 2B coolant pump [failed], (k) Loop 2 steam generator [normal water level], (l) Loop 2 steam generator [collapsed water level].

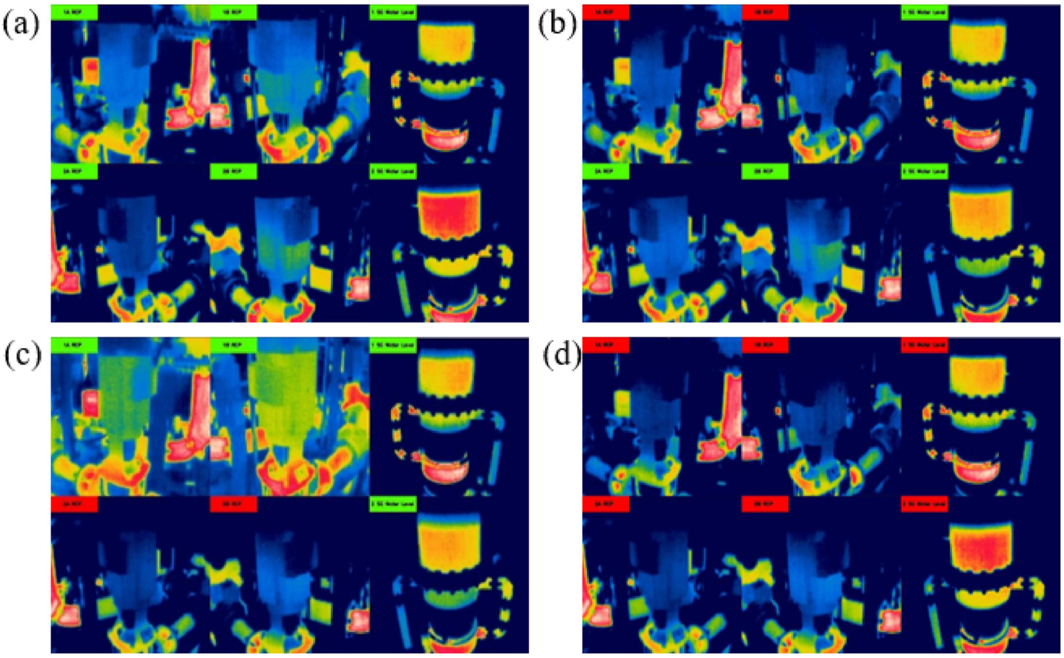

Fig. 8. Combined thermal images composed of diagnosed components in the early stages of accidents: (a) normal state, (b) RCP rotor seizure of Loop 1, (c) RCP rotor seizure of Loop 2, and (d) SBO.

performance for thermal imaging diagnosis with prompt classification. Therefore, the optimal model used for component diagnosis and accident classification was determined based on the diagnosis performance of the trained model for noise thermal image data that were not used for training, considering the inferior transmission condition. For performance evaluation based on the CNN structure, the thermal image was artificially manipulated by adding noise to 50% of the entire image pixel. 50% pixel of the image (R,G,B) was replaced by noise from Gaussian noise. 50% pixel of the image (R, G, B) was randomly selected. Fig. 10 represents the 50% noised thermal image used for performance evaluation. Table 9 summarizes the performance evaluation using thermal images that were not used for learning. AlexNet and all of the ANNs, which performed poorly on clear thermal images, were classified only as normal or abnormal. Although the CNN architectures that performed well on the clean thermal image classification showed good performance on the noisy thermal image, ResNet 18 exhibited better performance on the noisy thermal image than ResNet 34. Thus, it was concluded that the performance of the structure may change depending on the data. Nevertheless, GoogLeNet showed high performance for thermal image classification about the conditions considered in this study. Therefore, the optimal hyperparameter selection and validation were carried out based on GoogLeNet.

3.2.2. Validation of the deep learning model

As the training of the model was conducted with a small number of thermal images, k-fold cross-validation was performed to determine whether the model was biased based on the composition of the dataset, and the results are presented in Table 10. The model showed good performance regardless of the configuration of the dataset. However, when $k = 2$, the model performance deteriorated because the training dataset was too small to extract the features of the thermal images. Nevertheless, the model exhibited good performance.

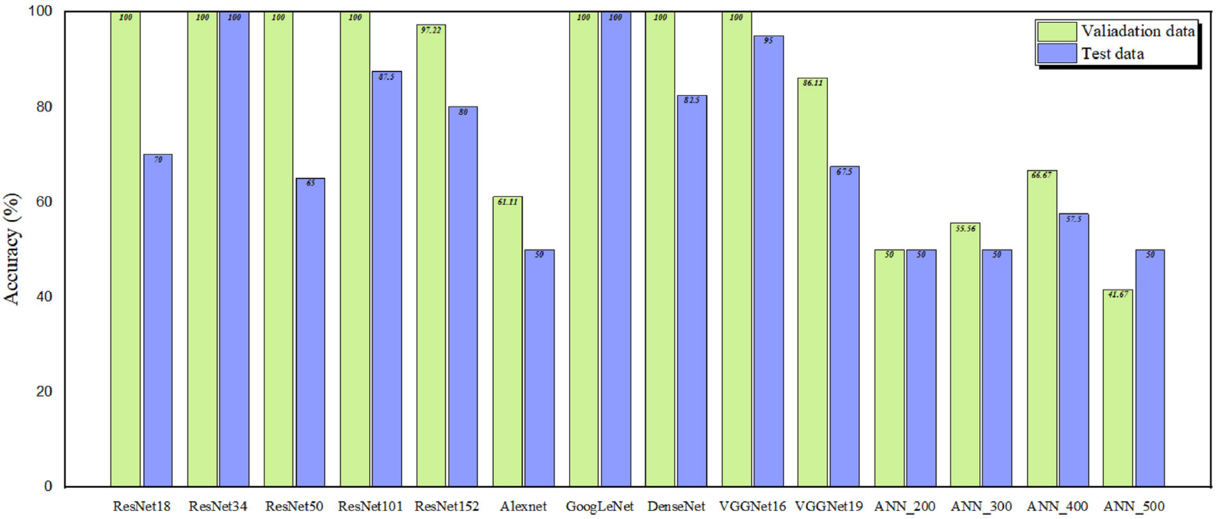

Fig. 9. Comparison of validation and test accuracies for an IR thermal image with different CNN architectures.

Table 7
Losses of training, validation, and test data and the average test time per image for different CNN architectures.

	Training loss	Validation loss	Test loss	Test time (sec)
ResNet18	5.2E-05	9.2E-03	2.1	$0.0436^{+0.0000}_{-0.0021}$
ResNet34	1.8E-04	3.6E-03	2.0E-02	$0.0694^{+0.0006}_{-0.0003}$
ResNet50	8.0E-05	5.3E-03	2.8	$0.0828^{+0.0008}_{-0.0025}$
ResNet101	3.1E-05	1.5E-01	9.9E-01	$0.1380^{+0.0015}_{-0.0030}$
ResNet152	2.3E-01	5.2E-01	4.2E-01	$0.1955^{+0.0001}_{-0.0004}$
AlexNet	7.0E-01	6.9E-01	7.1E-01	$0.0234^{+0.0006}_{-0.0022}$
GoogLeNet	1.6E-04	1.4E-04	1.4E-04	$0.0533^{+0.0005}_{-0.0003}$
DenseNet	3.1E-04	9.7E-04	1.1	$0.0701^{+0.0028}_{-0.0019}$
VGGNet16	1.0E-05	1.0E-05	4.9E-01	$0.0515^{+0.0003}_{-0.0003}$
VGGNet19	3.6E-01	3.0E-01	3.5E-01	$0.0561^{+0.0004}_{-0.0002}$
ANN_200	8.1E-01	8.1E-01	8.1E-01	$0.0154^{+0.0001}_{-0.0000}$
ANN_300	8.3E-01	7.6E-01	8.1E-01	$0.0163^{+0.0004}_{-0.0004}$
ANN_400	8.0E-01	6.5E-01	7.4E-01	$0.0199^{+0.0010}_{-0.0011}$
ANN_500	7.9E-01	9.0E-01	8.1E-01	$0.0218^{+0.0019}_{-0.0004}$

3.2.3. Grad-CAM

Grad-CAM was used to confirm the feature map that the deep learning model mainly used for training in identifying the defects of each component. Fig. 11 represents the thermal image of the steam generator and pump, the heat maps obtained through Grad-CAM, and the combined images. The steam generator water level diagnosis model mainly conjugates the temperature change of the upper part when checking the water level of the steam generator, and sub-confirms the temperature change of the entire steam generator. In the case of the pump diagnostic model, the thermal change of the upper part and the central part of the pump was mainly conjugated. However, because the data for pump diagnosis is with the thermal image of the surrounding environment, the pump diagnosis was conducted by reflecting the surrounding thermal change. In the case of the pump diagnosis model, the performance was superior to that of the steam generator level prediction model. Therefore, the environment temperature change can help improve the performance of diagnosis for main component. Both the steam generator water level diagnostic model and the pump diagnostic model focused on the temperature change of each component to confirm that the training proceeds. Hence, the model was trained through a proper feature map.

Table 8
Performance evaluation metrics for test datasets with different CNN architectures.

	Accuracy	Precision	Recall	F1 Score
ResNet18	0.700	0.702	0.700	0.701
ResNet34	1.000	1.000	1.000	1.000
ResNet50	0.650	0.665	0.650	0.657
ResNet101	0.875	0.900	0.875	0.887
ResNet152	0.800	0.830	0.800	0.815
AlexNet	0.500	0.250	0.500	0.333
GoogLeNet	1.000	1.000	1.000	1.000
DenseNet	0.825	0.847	0.825	0.836
VGGNet16	0.950	0.955	0.950	0.952
VGGNet19	0.800	0.830	0.800	0.815
ANN_200	0.500	0.250	0.500	0.333
ANN_300	0.500	0.250	0.500	0.333
ANN_400	0.55	0.567	0.55	0.528
ANN_500	0.500	0.250	0.500	0.333

3.2.4. Result of diagnosis

Fig. 12 illustrates the component diagnosis result from the optimal model. Fig. 12 (a) and (b) represent the diagnosis results of RCP in normal operating and malfunction conditions. and Fig. 12 (c) and (d) represent the diagnosis results of steam generators

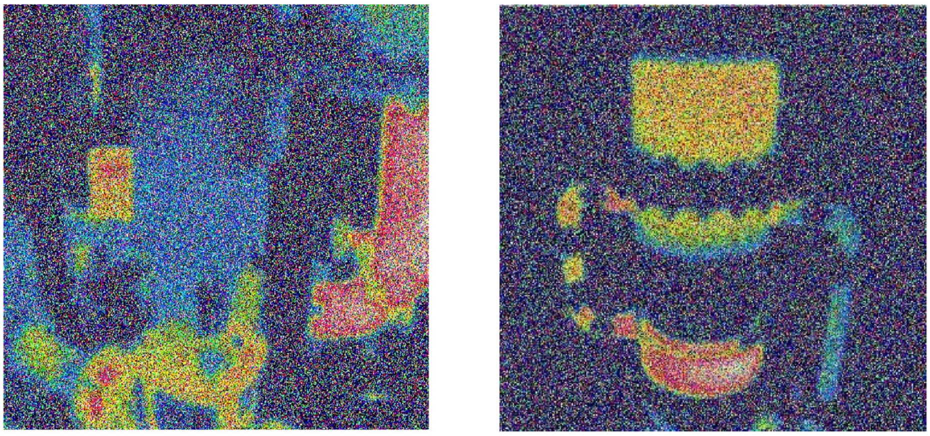

Fig. 10. The 50% pixel noised thermal image of RCP and the steam generator.

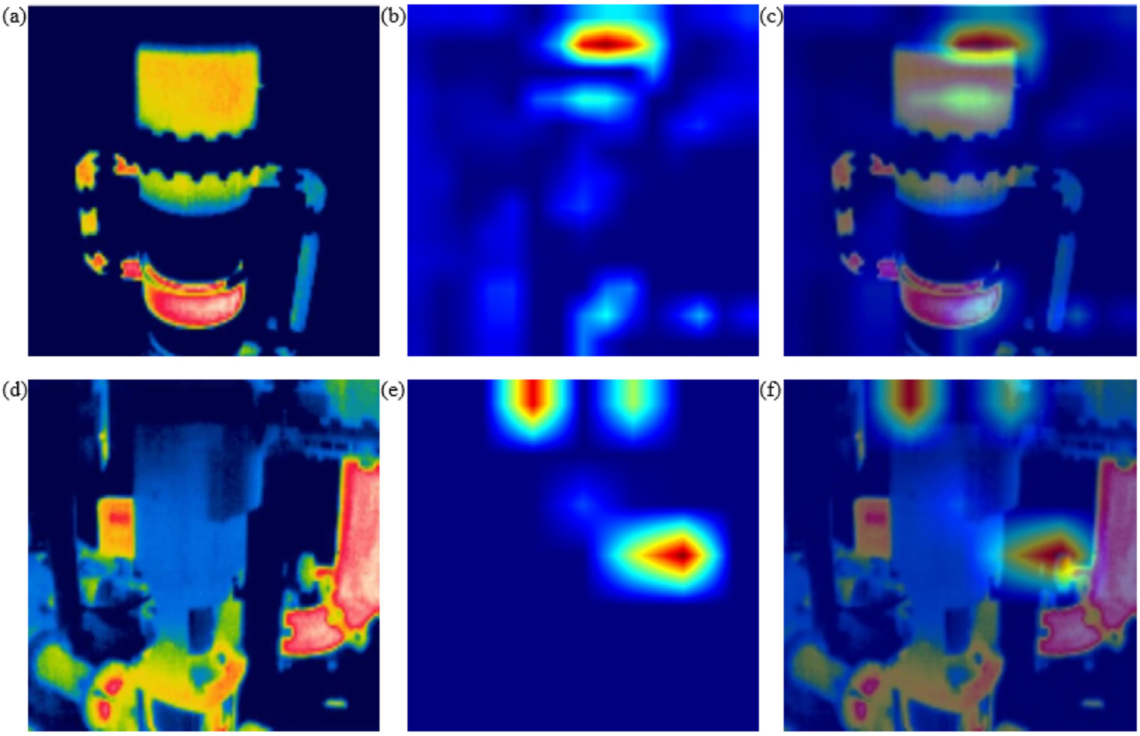

Fig. 11. Visualization of class activation maps: (a) thermal image of steam generator, (b) Grad-CAM for steam generator, (c) combined image for steam generator (e) thermal image of RCP, (b) Grad-CAM for RCP, (c) combined image for RCP.

Table 9
Performance evaluation metrics for untrained noise images with different CNN architectures.

	Accuracy	Precision	Recall	F1 Score
ResNet18	0.940	0.943	0.940	0.941
ResNet34	0.930	0.939	0.930	0.934
ResNet50	0.805	0.819	0.805	0.812
ResNet101	0.900	0.906	0.900	0.903
ResNet152	0.770	0.828	0.770	0.798
AlexNet	0.50	0.250	0.500	0.333
GoogLeNet	0.980	0.980	0.980	0.980
DenseNet	0.905	0.906	0.905	0.906
VGGNet16	0.945	0.945	0.945	0.945
VGGNet19	0.720	0.739	0.720	0.729
ANN_200	0.500	0.250	0.500	0.333
ANN_300	0.500	0.250	0.500	0.333
ANN_400	0.525	0.533	0.525	0.529
ANN_500	0.500	0.250	0.500	0.333

depending on the water level. Fig. 13 illustrated the accident classification result in accordance with each condition. The model for pump diagnosis and accident classification outperformed the model described above. The pump diagnosis had comparable times per thermal image as a result of the identical pixel size. The accident classification time per thermal image was 0.054825 s, and the

Table 10
Performance evaluation metrics under k-fold cross-validation.

# of Fold	Accuracy	Precision	Recall	F1 Score
2	0.995	1.000	0.990	0.995
5	1.000	1.000	1.000	1.000
8	1.000	1.000	1.000	1.000
10	1.000	1.000	1.000	1.000

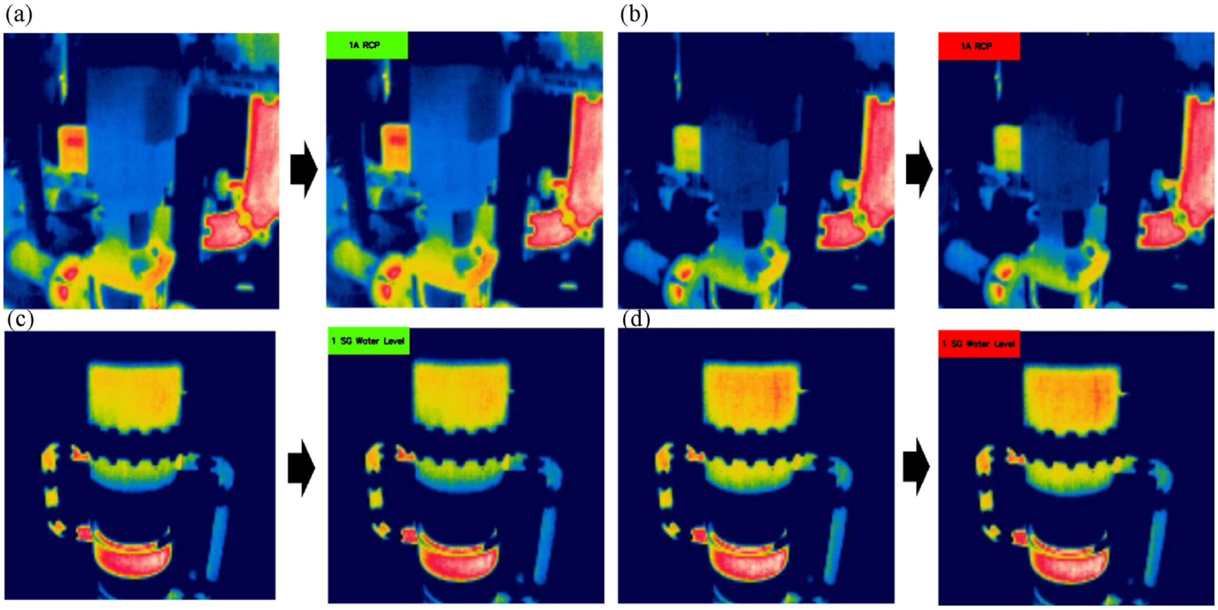

Fig. 12. Thermal images acquired by IR thermal camera (a) normal RCP, (b) RCP malfunction, (c) at the normal range of water level in the secondary side of the steam generator, and (d) collapsed water level less than the normal range.

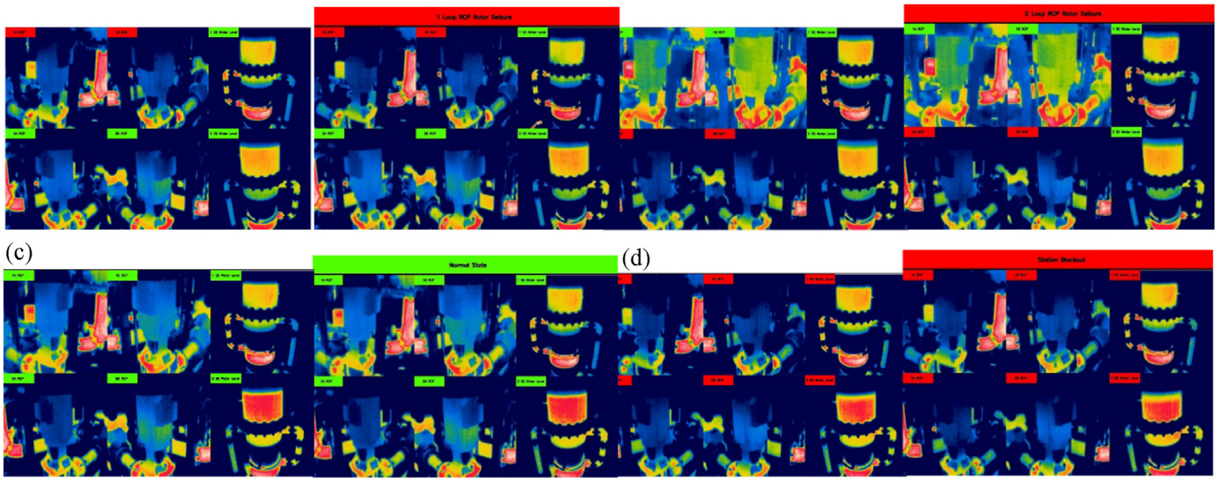

Fig. 13. Thermal images in the early stages of accidents (a) RCP rotor seizure of loop 1, (b) RCP rotor seizure of loop 2, (c) normal state, and (d) station blackout.

average time for component diagnosis and accident classification was 0.117248 s. Therefore, the system-scale diagnosis using thermal images showed good performance in quasi-real-time.

4. Conclusion

This study proposes a method for diagnosing components and the system scale by applying deep learning to images from non-contact IR thermal cameras. The proposed method can more intuitively identify fault locations than existing data-dependent methods. In addition, the possibility of misdiagnosis by the system operator can be reduced by applying deep learning. A thermal image database from URI-LO was utilized for system-scale diagnosis; the accident simulations were verified by the thermal-hydraulic analysis code to ensure that the conditions of the URI-LO experiment represented the NPP conditions. The thermal images acquired in the URI-LO accident experiment were reliable as an NPP diagnostic dataset because the results of the experiments showed similar behavior to that of the thermal-hydraulic analysis code. Because a high-performance/high-resolution IR camera is difficult to install, has difficulty transmitting data, and is expensive, compact IR thermal cameras with a Raspberry Pi were employed for system-scale diagnosis to facilitate installation, data transmission, and cost-effectiveness. By applying a CNN classification algorithm, which has excellent image processing capability, accurate and prompt component diagnosis and accident classification could be realized. Compared with other CNN classification architectures, GoogLeNet achieved prompt and accurate classification of thermal images for the condition considered in this study. Based on the selection of the optimal model and learning conditions, the deep-learning-based system-scale diagnosis with the thermal image method could classify steady-state, DBA, and BDBA conditions in quasi-real-time with 98%–100% accuracy. The component diagnosis model was able to distinguish whether the water level had collapsed and whether the system was operating normally. The proposed system diagnostic method can provide good performance for component diagnosis and accident classification for any system composed of numerous components, in addition to the NPPs considered in this study. However, the diagnosis performance of more components, composed of the systems, should be confirmed to apply this technology to actual NPPs or another system, since this study has only proven the diagnosis performance of pumps and the water level of the steam generator. The schematic of the steam generator and the pump would be considered different from URI-LO when applied to nuclear power plants. In that case, the training should be conducted considering the newly applied system. A similar performance could be maintained if transfer learning with the deep learning model utilized in this study. Furthermore, more accidents should be considered from another integral test facility because URI-LO was constructed for RCP rotor seizure and SBO. Real-time diagnosis is expected based on performance enhancement and improvements in data processing in the future.

Declaration of competing interest

The authors declare that they have no known competing financial interests or personal relationships that could have appeared to influence the work reported in this paper.

Acknowledgment

This work was supported by the A.I. Incubation Project Fund (1.220043.01) of UNIST(Ulsan national Institute of Science & Technology), and partly by the National Research Foundation of Korea(NRF) grant funded by the Korea government(MSIT) (No.2021M2D2A1A03048950) and KOREA HYDRO & NUCLEAR POWER CO., LTD (No. 2020-Tech-17).

References

[1] K. Moshkbar-Bakhsayesh, M. Ghofrani, Transient identification in nuclear power plants: a review, Prog. Nucl. Energy 67 (2013) 23–32.
[2] M.M. Najafabadi, F. Villanustre, T.M. Khoshgoftaar, Deep learning applications and challenges in big data analytics, Journal of Big Data 2 (2015) 1.
[3] H.M. Park, J.H. Lee, K, D. Kim, Wall temperature prediction at critical heat flux using a machine learning model, Ann. Nucl. Energy 141 (2020), 107334.
[4] T.V. Santosh, G. Vinod, R.K. Saraf, A.K. Ghosh, H.S. Kushwaha, Application of artificial neural networks to nuclear power plant transient diagnosis, Reliab. Eng. Syst. Saf. 92 (2007) 1468–1472.
[5] H.A. Saeed, M. Peng, H. Wang, B. Zhang, Novel fault diagnosis scheme utilizing deep learning networks, Prog. Nucl. Energy 118 (2020), 103066.
[6] G. Lee, S.J. Lee, C. Lee, A convolutional neural network model for abnormality diagnosis in a nuclear power plant, Appl. Soft Comput. 99 (2020), 106874.
[7] S. Bagavathiappan, B.B. Lahiri, T. Saravanan, J. Philip, T. Jayakumar, Infrared thermography for condition monitoring – a review, Infrared Phys. Technol. 60 (2013) 35–55.
[8] S. Albawi, T.A. Mohammed, S. Al-Zawi, Understanding of a convolutional neural network, in: *2017 International Conference On Engineering And Technology (ICET)*, Antalya, Turkey, 2017.
[9] O. Janssens, R. Van de Walle, M. Loccufier, S. Van Hoecke, Deep learning for infrared thermal image based machine health monitoring, IEEE/ASME Transactions and Mechatronics 99 (2018) 151–159.
[10] J.S. Kim, K.N. Choi, S.W. Kang, Infrared thermal image-based sustainable fault detection for electrical facilities, Sustainability 13 (2021) 557.
[11] A. Nasiri, A. Taheri-Garavand, M. Omid, G.M. Carlomagno, S.W. Kang, Intelligent fault diagnosis of cooling radiator based on deep learning analysis of infrared thermal images, Appl. Therm. Eng. 163 (2019), 114410.
[12] J. Yang, W. Wang, G. Lin, Q. Li, Y. Sun, Y. Sun, Infrared thermal imaging-based crack detection using deep learning, in: IEEE Access, vol. 7, 2019, pp. 182060–182077.
[13] K.M. Kim, I.C. Bang, Design and operation of the transparent integral effect test facility, URI-LO for nuclear innovation platform, Nucl. Eng. Technol. 53 (2021) 776–792.
[14] M. Ishii, I. Kataoka, Scaling laws for thermal-hydraulic system under single phase and two-phase natural circulation, Nucl. Eng. Des. 81 (1984) 411–425.
[15] K.M. Kim, I.C. Bang, Integral Effect Test in Visualization Basis 3D Printed Test Facility for Improved Application of Innovative Technology, International Topical Meeting on Nuclear Reactor Thermal Hydraulics, NURETH-18), Portland, USA, 2019.
[16] X.G. Yu, H.S. Park, Y.S. Kim, K.H. Kang, S. Cho, K.Y. Choi, Systematic analysis of a station blackout scenario for APR1400 with test facility ATLAS and MARS code from scaling viewpoint, Nucl. Eng. Des. 259 (2013) 205–220.
[17] K.H. Lee, B.U. Bae, Y.S. Kim, B.J. Yun, J.H. Chun, G.C. Park, An integral loop test and MARS code analysis for a DVI line break LOCA in the APR1400, Nucl. Eng. Des. 238 (2008) 3336–3347.
[18] S. Kim, H.Y. Jun, Analysis of an ATLAS 6-in. cold-leg break simulation with MARS code, Ann. Nucl. Energy 63 (2014) 268–275.
[19] S.Y. Park, K.I. Ahn, Comparative analysis of station blackout accident progression in typical PWR, BWR, and PHWR, Nucl. Eng. Technol. 44 (2012) 311–322.
[20] A. Prošek, L. Cizelj, Long-term station blackout accident analysis of a PWR with RELAP5/MOD3.3, Science and Technology of Nuclear Installations 2013 (2013), 851987.
[21] A. Canziani, A. Paszke, E. Culurciello, An Analysis of Deep Neural Network Models for Practical Application, 2016, 07678 arXiv preprint arXic:1605.
[22] A. Krizhevsky, I. Sutskever, G. Hinton, Imagenet classification with deep convolutional neural networks? Communications of the ACM 60 (6) (2012) 84–90.
[23] C. Szegedy, W. Liu, Y. Jia, P. Sermanet, S. Reed, D. Anguelov, D. Erhan, V. Vanhoucke, A. Rabinovich, Going deeper with convolutions, in: Proceedings of the IEEE Conference on Computer Vision and Pattern Recognition, CVPR), Boston, USA, 2015.
[24] K. Simonyan, A. Zisserman, Very Deep Convolutional Networks for Large-Scale Image Recognition, 2014 arXiv:1409.1556.
[25] K. He, X. Zhang, S. Ren, J. Sun, Deep residual learning for image recognition, in: Proceedings of the IEEE Conference on Computer Vision and Pattern Recognition (CVPR), Las Vegas, Nevada, 2016.
[26] G. Huang, Z. Liu, L. Maaten, K.Q. Weinberger, Densely connected convolutional networks, in: Proceedings of the IEEE Conference on Computer Vision and Pattern Recognition, CVPR), Honolulu, Hawaii, 2017.
[27] S. Ruder, An Overview of Gradient Descent Optimization Algorithms, 2016 arXiv preprint arXiv:1609.04747.
[28] C. Sammut, G.I. Webb (Eds.), Encyclopedia of Machine Learning, Springer, New York, 2011.
[29] M. Vakili, M. Ghamsari, M. Rezaei, Performance Analysis and Comparison of Machine and Deep Learning Algorithms for IoT Data Classification, 2020 arXiv preprint arXiv:2001.09636.
[30] R.R. Selvaraju, M. Cogswell, A. Das, R. Vedantam, D. Parikh, D. Batra, Grad-cam: visual explanations from deep networks via gradient-based localization, in: Proceedings of the IEEE International Conference on Computer Vision, 2017, pp. 618–626.